Department of Physics and Astronomy
University of Heidelberg

Bachelor Thesis in Physics
submitted by

Benedikt Herwerth

born in Freiburg im Breisgau (Germany)

2011

Dynamics of Quantum Reflection in Atom-Surface Interactions

This Bachelor Thesis has been carried out by Benedikt Herwerth at the
Institute for Theoretical Physics in Heidelberg
under the supervision of
Dr. Sandro Wimberger

Dynamics of Quantum Reflection in Atom-Surface Interactions

Quantum reflection, the reflection of a particle on an attractive potential, is a quantum mechanical phenomenon without classical analogue. A good framework to study it, both experimentally and theoretically, are atom-surface interactions. In this project, a method to integrate the one-dimensional time-dependent Schrödinger equation is applied to a $-C_3/x^3$-potential as occurring in atom-surface interactions. The method is tested by comparing the results to numerical calculations within the time-independent Schrödinger equation. Consequently, a dynamically influenced process is studied: the reflection of a particle on a harmonically oscillating surface. It is shown that in the momentum distribution of the reflected particle, in addition to the elastic peak, side peaks become visible. Being directly connected to the oscillating frequency, these arise from the energy transfer between the particle and the oscillating surface.

Dynamik der Quantenreflexion in Atom-Oberflächen-Wechselwirkungen

Quantenreflexion, die Reflexion eines Teilchens an einem anziehenden Potential, ist ein quantenmechanisches Phänomen ohne klassisches Analogon. Ein guter Rahmen, um diese experimentell und theoretisch zu untersuchen, sind Atom-Oberflächen-Wechselwirkungen. In diesem Projekt wird eine Methode zur Integration der zeitabhängigen Schrödingergleichung auf ein $-C_3/x^3$-Potential angewendet, wie es in Atom-Oberflächen-Wechselwirkungen vorkommt. Die Methode wird getestet, indem die Resultate mit numerischen Rechnungen im Rahmen der zeitunabhängigen Schrödinger Gleichung verglichen werden. Infolgedessen wird ein dynamisch beeinflusster Prozess untersucht: Die Reflexion eines Teilchens an einer harmonisch oszillierenden Oberfläche. Es wird gezeigt, dass in der Impulsverteilung des reflektierten Teilchens, neben dem elastischen Peak, Seitenbänder sichtbar werden. Diese sind direkt mit der Oszillationsfrequenz verknüpft und entsprechen einem Energieaustausch zwischen dem Teilchen und der Oberfläche.

Contents

1 Introduction **6**
1.1 Reflectivity . . . 6
1.2 Atom-Surface Interactions . . . 7

2 Methods **9**
2.1 Continuation of the Potential at the Origin . . . 9
2.2 Time-Dependent Numerical Methods . . . 10
2.3 Time-Independent Calculation of the Reflectivity . . . 11
2.4 Discussion of the Continuations . . . 11

3 Results **15**
3.1 Static Potential . . . 15
3.1.1 Time Evolution of a Wave Packet . . . 15
3.1.2 Optimization of Numerical Parameters . . . 15
3.1.3 Absorbing Boundaries . . . 16
3.1.4 Calculation of the Reflectivity and Comparison of Methods . . . 19
3.2 Time-Dependent Potential . . . 21
3.2.1 Momentum Distribution . . . 21
3.2.2 Sidebands in the Energy Distribution . . . 23
3.2.3 Optimization of Numerical Parameters . . . 24
3.2.4 Limit of Small x_0 . . . 25

4 Conclusion and Perspectives **29**

A Crank-Nichelson Method for the Schrödinger Equation **31**

B Time-Independent Calculation of the Reflectivity **32**

C Computational Costs: Computation Time **34**

D Retarded Potential **35**

E References **37**

1 Introduction

In the past decade, experimental advances in the cooling of atoms have led to an increased interest in the reflection of atoms on a surface: By achieving slow incident velocities, the reflectivity due to the long-range attractive part of the atom-surface interaction became experimentally accessible [1]. Such a process, when particles are reflected on the attractive part of a potential, is referred to as *quantum reflection*. Quantum reflection is, for example, proposed to enhance the trapping of atoms [2]. Even in itself, it appears to be an interesting phenomenon being called "paradoxical" in a recent article [3], since it does not have a classical analogue.

In this project, a method to integrate the time-dependent Schrödinger equation was applied to a reflection process of an atom on a surface. To overcome numerical difficulties, absorbing boundaries were introduced. The accuracy of the method was shown by comparison to results obtained by integrating the time-independent Schrödinger equation. Motivated by commercially available membranes [4], the method was then applied to the reflection of an atom on a harmonically oscillating surface.

1.1 Reflectivity

In a situation, where an asymptotically free particle enters some localized region of interaction, the reflectivity R can be defined as the probability that the particle is reflected after the interaction. Given a one-dimensional potential $V(x)$, which fulfills $V(x) \approx 0$ for $x > a$, and given an initial state $\psi_i(x)$, which is prepared such that an interaction takes place at times around t_0, and a final state $\psi_f(x)$ for $t \gg t_0$, the reflectivity is

$$R = \int_{x>a} |\psi_f(x)|^2 \, \mathrm{d}x. \tag{1}$$

When a beam of particles is exposed to the interaction, the reflectivity is equal to the ratio of the reflected flux to the incoming flux of particles. This second approach is useful for a time-independent treatment of the problem: Given the state $\phi(x)$ as a solution to the *stationary* Schrödinger equation for a particle with mass m and energy E and a potential fulfilling $V(x) \approx 0$ for $x > a$, we have

$$\phi(x) = Ae^{ikx} + Be^{-ikx} \text{ for } x > a, \tag{2}$$

where $A, B \in \mathbb{C}$ and $k = \sqrt{2mE/\hbar^2}$. The term $\phi_+(x) = Ae^{ikx}$ represents a right-going particle, whereas the term $\phi_-(x) = Be^{-ikx}$ represents a left-going particle[1]. Assuming that the incoming particle is represented by the left-going wave ϕ_-, the reflectivity can be calculated as the ratio of the associated probability fluxes [5, p. 75]

$$j_{\phi_\pm} = \frac{\hbar}{m} \operatorname{Im}(\phi_\pm^* \frac{\mathrm{d}\phi_\pm}{\mathrm{d}x}) \tag{3}$$

as

$$R = |\frac{j_{\phi_+}}{j_{\phi_-}}| = |\frac{A}{B}|^2. \tag{4}$$

Here, the reflectivity was calculated both by a time-independent calculation according to Eq. (4) and by a time-dependent calculation according to Eq. (1).

1.2 Atom-Surface Interactions

The interaction potential between a neutral atom and a surface is characterized by a repulsive regime, which applies for very short distances from the surface, and a long-range attractive regime. A sketch of the interaction potential can be found in Fig. 1.

The fact that the interaction becomes repulsive for short distances can be motivated in terms of the Pauli principle: As Fermions, the electrons surrounding the atom and the electrons in the surface cannot be in the same state. In coordinate space, this leads to a favored spatial separation of the atom from the surface, which is expressed by a repulsive potential [6].

The attractive part can be understood qualitatively as follows: The atom is spontaneously polarized by the radiation field, which, for a conducting surface, gives rise to a mirror dipole in the surface. The attraction is due to the interaction of the atom with its mirror dipole. For large distances, retardation effects have to be taken into account, which effectively weaken the interaction strength. This attractive interaction can be described by

$$V(x) = -\frac{C_4}{x^3(x+l)}, \tag{5}$$

[1] This interpretation is motivated by the fact that $\phi_\pm$ are (generalized) eigenstates to the momentum operator with eigenvalues $\hbar k$ and $-\hbar k$, respectively.

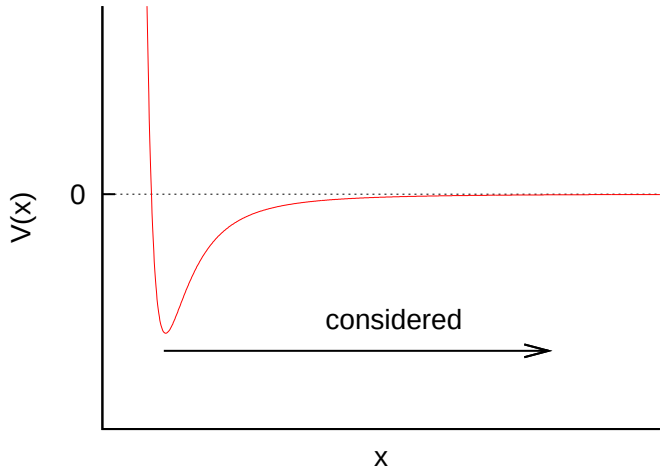

Figure 1: Atom-surface interaction potential (arbitrary units). Here, only the attractive part ($-C_3/x^3$) is considered.

where C_4 is a constant, x is the distance of the atom to the surface and l is the reduced wavelength of the atomic transition. This expression can be found in [7], where also more sophisticated expressions are considered. The short range limit ($x \ll l$) of this potential is $V(x) = -C_3/x^3$ with $C_3 = C_4/l$.

Here, the values

$$C_3 = \quad 4 \cdot 10^{-50} Jm^3 \quad (0.062 a.u.) \tag{6}$$

$$m = 5.00823 \cdot 10^{-27} kg (3.01603 u) \tag{7}$$

were used for all calculations, where m is the mass of ^3He [8]. The value of C_3 was taken from [7] and corresponds to the interaction of helium with a gold surface. For all numerical calculations, only the $-C_3/x^3$-potential was taken into account. In appendix D, it was checked that the method applies to the full potential given in Eq. (5).

2 Methods

The reflectivity was calculated numerically by an integration of the *stationary* Schrödinger equation and by integrating the *time-dependent* Schrödinger equation. In this section, the used numerical methods are described.

2.1 Continuation of the Potential at the Origin

Let us first clarify the role of the singularity of the $-C_3/x^3$-potential at the origin and how it was dealt with it in the numerical treatment of the problem.

In order to calculate the reflectivity for the *quantum reflection*, only the attractive part of the interaction potential was taken into account, i.e. $-C_3/x^3$. To avoid the singularity at the origin, the potential was cut at $x_0 > 0$ and suitably continued for $x \leq x_0$. This continuation allows the part of the wave function, which is not reflected in the region $x \geq x_0$, to move further to $x \to -\infty$. The reflectivity was then calculated for different values of x_0. It was assumed that in the limit $x_0 \to 0$ the reflectivity reaches a value which is independent of the precise form of the continuation and which represents the reflectivity of the quantum reflection for the actual potential. This assumption is supported by time-independent calculations, which were carried out using $V(x) = -C_3/x^3$ for $x > x_0$ and the following continuations for $x \leq x_0$:

constant continuation:

$$V(x) = -\frac{C_3}{x_0^3} \tag{8}$$

linear continuation:

$$V(x) = -\frac{C_3}{x_0^3} + \frac{3C_3}{x_0^4}(x - x_0) \tag{9}$$

parabolic continuation:

$$V(x) = \begin{cases} \frac{-C_3}{x_0^3} + 3\frac{C_3}{x_0^4}(x - x_0) + \frac{3C_3}{2x_0^5}(x - x_0)^2, & \text{if } 0 < x \leq x_0 \\ -\frac{5C_3}{2x_0^3}, & \text{if } x < 0 \end{cases} \tag{10}$$

All of these continuations ensure the continuity of the potential in x_0 and for the *linear* and the *parabolic* continuations, the derivative of $V(x)$ is also continuous in x_0. Fig. 2 contains a plot of the continuations.

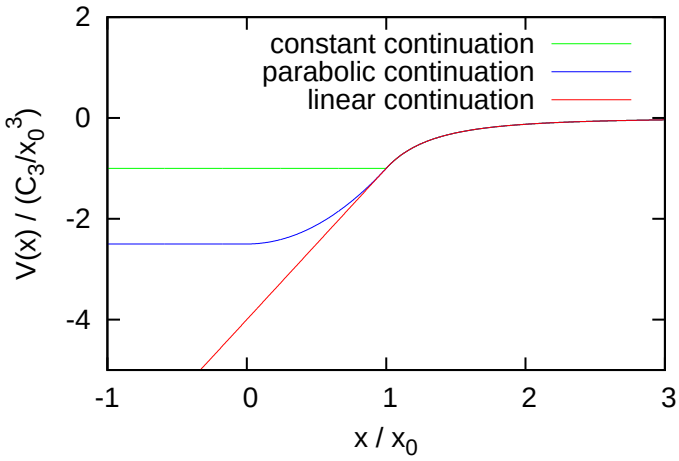

Figure 2: Different possibilities to continue the potential for $x < x_0$.

2.2 Time-Dependent Numerical Methods

The method used to solve the time-dependent Schrödinger equation with the Hamiltonian H is known as the "Crank-Nichelson"-method [9]. Numerically, the wave function at each time t is represented as a discrete vector of N-components, i.e. ψ_t is sampled on N grid points with an equidistant discretization step Δx. This *spatial discretization* implies that operators, which originally act on wave functions, need to be represented by $N \times N$-matrices. The optimal number of grid points N was found by a numerical analysis (section 3.1.2). After specifying an initial wave function, the time evolution is calculated in steps Δt in time. For each time step, the equation

$$(1 + iH\Delta t/2\hbar)\psi_{t+\Delta t} = (1 - iH\Delta t/2\hbar)\psi_t \tag{11}$$

has to be solved for $\psi_{t+\Delta t}$. The second derivative $\partial^2/\partial x^2$ contained in the Hamiltonian can be approximated by finite difference expressions. *Three-point* and *five-point* approximations of $\partial^2/\partial x^2$ were used, which give rise to either tridiagonal or five-diagonal matrices as representations of the operators in Eq. (11). Details on this numerical method are given in appendix A.

2.3 Time-Independent Calculation of the Reflectivity

The reflectivity was also calculated by a numerical integration of the time-independent Schrödinger equation

$$-\frac{\hbar^2}{2m}\frac{\mathrm{d}^2\psi}{\mathrm{d}x^2}(x) + V(x)\psi(x) = E\psi(x) \tag{12}$$

for a particle with mass m and energy $E > 0$. For the potential $V(x) = -C_3/x^3$ for $x > x_0$ with one of the continuations described above for $x \leq x_0$, the known analytical solutions of the continuations were used to define an initial condition $(\psi(x_i), \psi'(x_i))$. Here, ψ' denotes the derivative of the wave function. This initial condition was chosen such that the boundary condition for $x \to -\infty$ is respected, i.e. ψ represents an *outgoing* particle for $x \to -\infty$. Once the initial condition was specified, the wave function was calculated for $x > x_i$. For a sufficiently large value x_f, the potential vanishes approximately and the calculated wave function and its derivative, $(\psi(x_f), \psi'(x_f))$, were used to calculate the reflectivity by matching them to the sum of an incoming and an outgoing plane wave. Further details on this method are given in appendix B. The integrator *odeint* of the *SciPy*-software package [10] was used to calculate $(\psi(x_f), \psi'(x_f))$ numerically.

2.4 Discussion of the Continuations

Integrating the time-independent Schrödinger equation, the reflectivity was calculated for the different continuations of the potential as shown in Fig. 3. In these calculations, the connection point x_0 was varied.

Note that the reflectivity reaches a final value as x_0 approaches 0 and that this value is independent of the chosen form of the continuation. For all continuations, oscillations of the reflectivity as a function of x_0 are visible. These oscillations can be understood as follows: By cutting the potential at the point x_0, the "artificial" length scale x_0 is introduced. This parameter is physically equivalent to the potential energy $-C_3/x_0^3$ at that point, which determines the de Broglie wavelength of the particle,

$$\lambda_{dB}(x_0) = \frac{2\pi\hbar}{\sqrt{2m(E + C_3/x_0^3)}}. \tag{13}$$

For $C_3/x_0^3 \gg E$, the de Broglie wavelength depends on x_0 according to

$$\lambda_{dB}(x_0) \propto x_0^{3/2}. \tag{14}$$

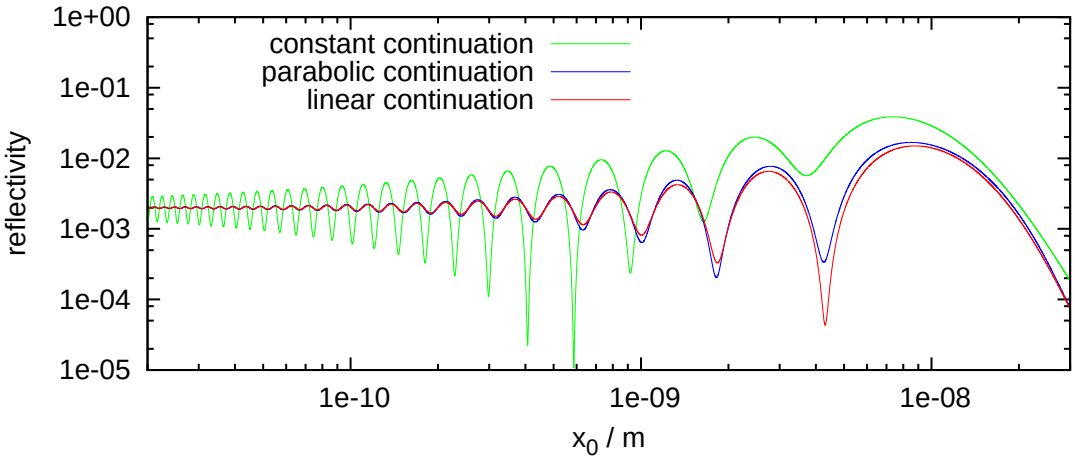

Figure 3: Reflectivity for different continuations of the potential.

It was found out, that the oscillations in the reflectivity follow the same scaling behavior (Fig. 4).

This shows that the oscillations of the reflectivity can indeed be interpreted as a result of the "artificial" connection at x_0. The fact that the oscillations are proportional to the de Broglie wavelength is plausible, since the reflections are due to the wave nature of the particle.

Note that the oscillations are of higher amplitude for the constant continuation than for the parabolic and the linear continuations. This can be seen as a consequence of the fact that the constant continuation is discontinuous in the derivative of the potential at x_0, whereas for the latter $V'(x)$ is continuous in x_0.

Based on these calculations, the decision was made to use the *parabolic continuation* for the *time-dependent* calculations. Compared to the constant continuation, it has clearly the advantage of converging faster against a final value of the reflectivity. At the same time, when compared to the linear continuation, it is advantageous because it remains bounded (its lowest value is $2.5 \cdot V(x_0)$).

By calculating the reflectivity as a function of the connection point x_0, the reflectivity for the full $-C_3/x^3$-potential (in the sense of the limit $x_0 \to 0$) could be extracted. Practically, this was done by averaging over periods of oscillations of R. As an illustration of this method, the reflectivity for the $-C_3/x^3$-potential was computed as a function of the initial velocity v of the incident particle (Fig. 5).

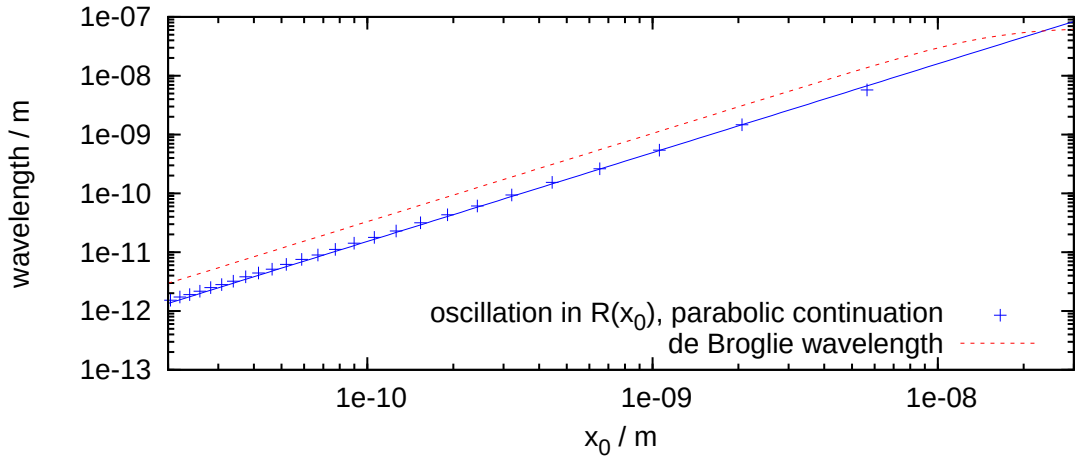

Figure 4: Oscillations of the reflectivity. For the parabolic continuation, the wavelengths are shown as a function of their position (distance between two subsequent maxima in $R(x_0)$ and their arithmetic mean). The solid line is a power law fit excluding the very right point. The fit yields $\lambda \propto x_0^{1.510\pm0.006}$, which agrees with the scaling behavior of the de Broglie wavelength. For the constant and the linear continuations, the wavelength follows the same behavior, which can also be seen in Fig. 3. Note that the scaling behavior $x_0^{3/2}$ of the de Broglie wavelength is the limiting case for $C_3/x_0^3 \gg E$. The right side of the plot marks the begin of this regime.

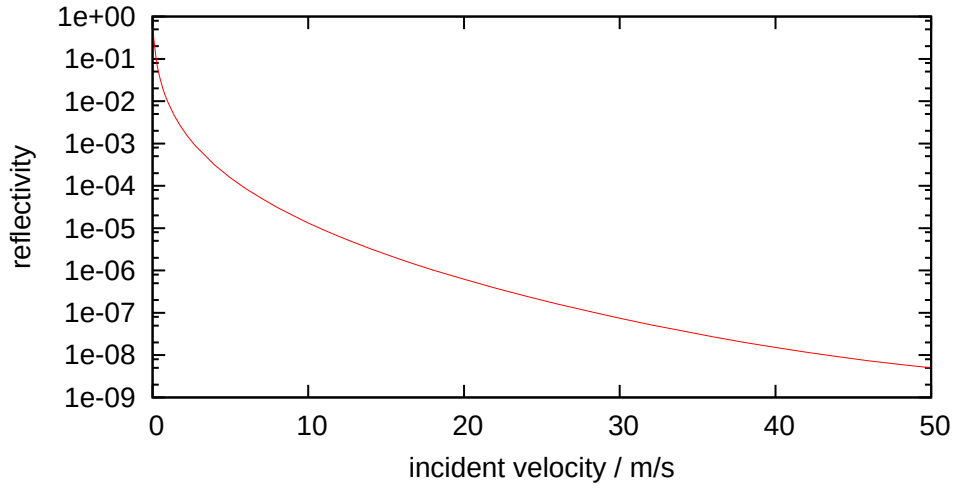

Figure 5: Calculated reflectivity of the $-C_3/x^3$-potential for ^3He as a function of the initial velocity. The reflectivity was computed by an integration of the time-independent Schrödinger equation with the linear continuation for the potential. For 60 velocities, it was averaged over two oscillations of $R(x_0)$ (see Fig. 3) for $2.00 \cdot 10^{-12}m < x_0 < 2.15 \cdot 10^{-12}m$, where 500 points of $R(x_0)$ were calculated.

3 Results

3.1 Static Potential

First, the method to integrate the *time-dependent* Schrödinger equation was applied to the $-C_3/x^3$ potential. The results were compared to those obtained by integrating the *time-independent* Schrödinger equation.

3.1.1 Time Evolution of a Wave Packet

In Fig. 6, the time evolution of a Gaussian wave packet is shown in coordinate and in momentum space. Here and in the following calculations, the initial, mean particle velocity is

$$v = -2m/s, \tag{15}$$

and the width of the initial wave packet[2] is

$$\sigma = 0.08\mu m. \tag{16}$$

The momentum distribution $|\psi(k)|^2$ was obtained from the coordinate wave function $\psi(x)$ by a discrete Fourier transform (*fast Fourier transform* [9, p. 390 - 395]). Note that the momentum of the incoming particle was chosen to be *negative*, whereas the reflected particle has a *positive* momentum.

3.1.2 Optimization of Numerical Parameters

The numerical parameters Δx (spatial step size) and Δt (step size in time) have to be chosen such that the obtained results do not depend on their values. Usually, this independence is expected for small values of Δx and Δt. At the same time, it is desirable to keep them as large as possible, in order to limit numerical costs.

Fig. 7 shows how the calculated value of the reflectivity depends on Δx and Δt. The requested independence is reached if the number of grid points exceeds 2^{16} on a box of size $16\mu m$ and $\Delta t \leq 2 \cdot 10^{-10}s$. This optimization was carried out with a connection point of $x_0 = 7.38 \cdot 10^{-9}m$. Even though the independence on the numerical parameters was reached, a deviation of approximately 0.1% compared to the time-independent calculation remained. This deviation expresses the limits of

[2] standard deviation of the Gaussian $|\psi(x, t = 0)|^2$

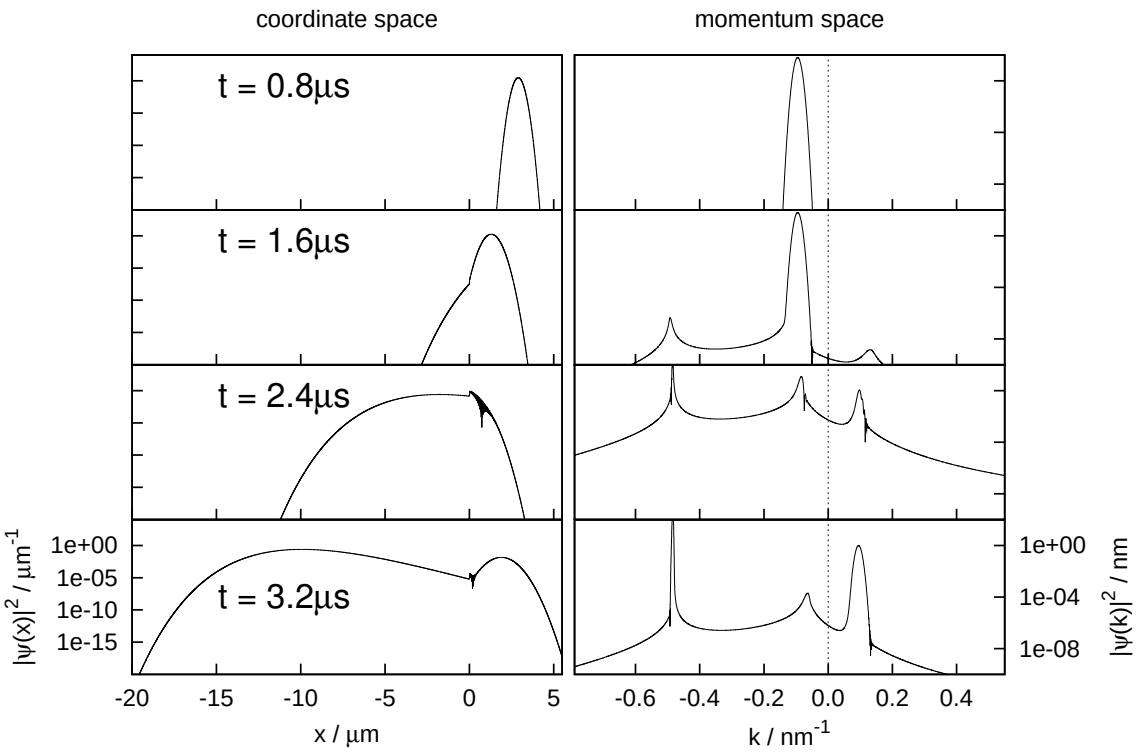

Figure 6: Evolution of a Gaussian wave packet in the potential. At t = 0, a Gaussian wave packet with width $\sigma = 0.08\mu m$ and mean velocity $v = -2m/s$ is placed at $x = 4.5\mu m$. The probability densities $|\psi(x)|^2$ and $|\psi(k)|^2$ are shown at different instants of time. At $t = 2.4\mu s$, the separation of a transmitted (negative momentum) and a reflected part (positive momentum) is visible. (Numerical parameters: Box size – $25.6\mu m$, $N = 2^{17}$ grid points, $\Delta t = 2 \cdot 10^{-10} s$).

the used numerical method. The results of this optimization were taken as a starting point for further calculations.

3.1.3 Absorbing Boundaries

As the connection point x_0 reaches lower values, the transmitted particle experiences a larger difference in potential energy. This increases its momentum, such that it hits the left boundary of the numerical grid. There, it is reflected, which causes unwanted effects. To avoid these reflections, one could in principle enlarge the size of the numerical box. But this is only possible to a certain degree, because it implies higher numerical costs. Therefore, *absorbing boundaries* were introduced. This made it possible to reach values of x_0 from which the final reflectivity could be calculated.

The following methods were compared:

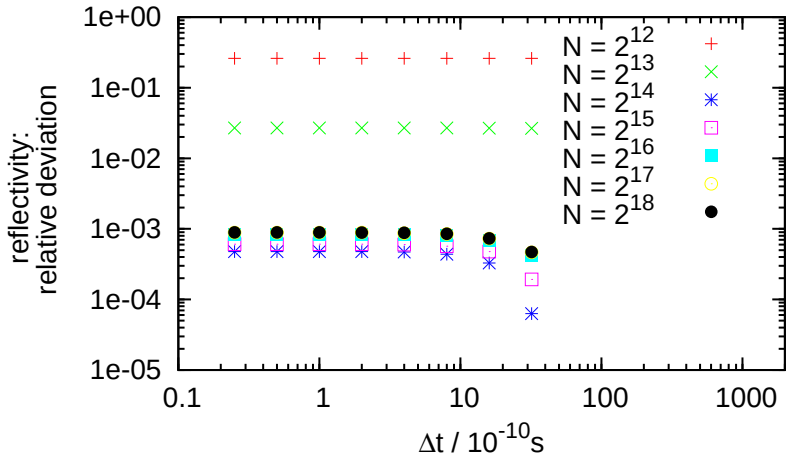

Figure 7: Variation of the numerical parameters: For a box size of $16\mu m$, the number of spatial grid points N and the temporal step size Δt was varied. The relative deviation of the calculated reflectivity to the value obtained by an integration of the stationary Schrödinger equation is shown on the vertical axis. The *five-point approximation* was used here.

- altering the differential equation for the wave function at the boundary, such that this is transparent for a wave with a specified momentum. This method was introduced by T. Shibata [11].
- filtering in coordinate space: The wave function is multiplied by a damping function $f(x)$ after each time step Δt:

$$\psi(x) \to f(x)\psi(x) \ . \tag{17}$$

- filtering in momentum space: The wave function in momentum space, which is obtained by a Fourier transform, is multiplied by a damping function, which suppresses unwanted momenta. The back-transformed coordinate wave function is propagated further in time.

In Fig. 8, the different methods are compared on the basis of the computed probability distribution $|\psi(x)|^2$ after the collision with the boundary. Judging from the obtained results, the *filtering in coordinate space*, which shows no visible reflections, is to be preferred. The slight reflections in the case of the boundary conditions according to T. Shibata can be understood in the following way: Since this method is based on an approximation of the dispersion relation of a free particle, it can only be transparent for momenta, where this approximation is good. The transmitted

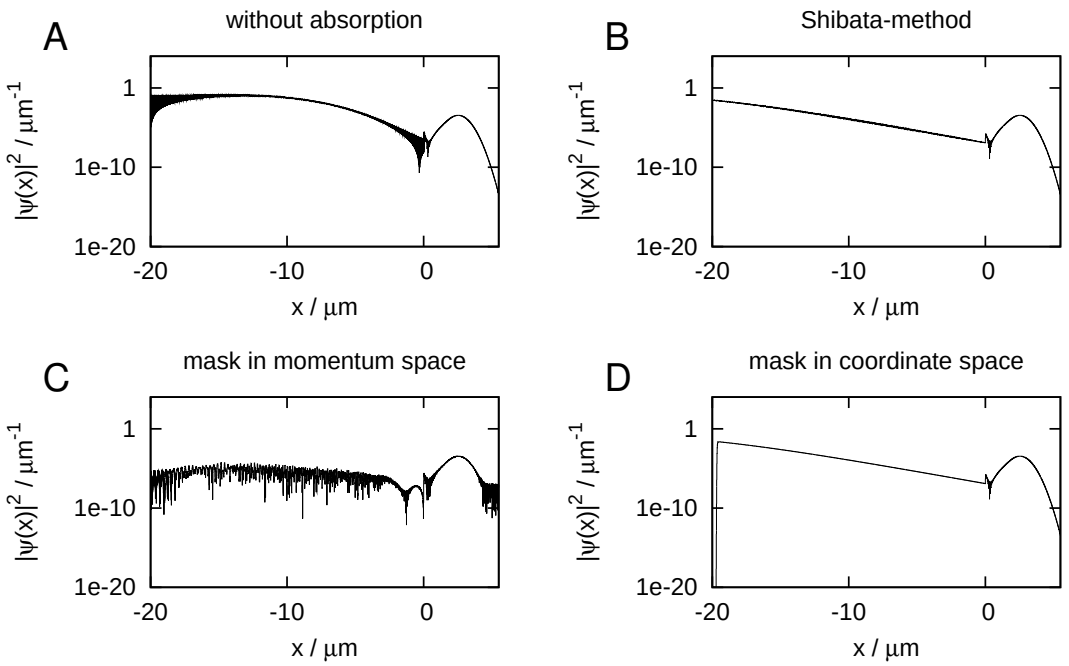

Figure 8: Comparison of different methods of absorption at the left boundary. In all panels, the probability distribution is shown at $t = 3.40\mu s$. At $t = 0$, a Gaussian wave packet with width $\sigma = 0.08\mu s$ and mean velocity $-2m/s$ was placed at $x = 4.5\mu m$. A: Without absorption, the spurious reflections are visible. B: Boundary conditions according to T. Shibata [11] were used. Slight reflections in the region $x < 0$ are visible. C: The Fourier transform of the wave function was multiplied by an absorbing mask after each 100th time step of width Δt. The used damping function cuts the transmitted part of the wave function. Spurious noise occurs at a high level in the probability distribution in coordinate space. D: The wave function was multiplied by an absorbing mask at the right boundary after each step Δt.

wave function contains a distribution of momenta and therefore some reflections occur from momenta not covered by the approximation. As the filtering in momentum space shows, the artificial modifications in momentum space give rise to non-local noisy structures in coordinate space. Apparently, the modifications in momentum space conflict with the time evolution. No better results could be obtained by performing the filtering after more or less steps Δt or by varying the form of the damping function.

For the above comparison and the following calculations, the damping function

$$f(x) = \frac{1}{\exp(-\frac{x-a}{d})+1}$$

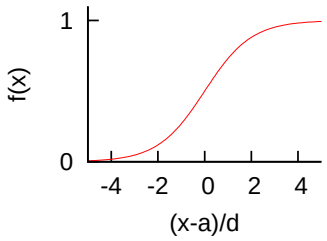

was used. Instead of specifying the parameters a and d directly, two properties of the damping function were fixed, which then uniquely defined a and d:

- definition of an "absorption area": If x_b is the lower boundary of the numerical grid, a point $c > x_b$ was specified such that for $x > c$: $|f(x) - 1| < 10^{-16}$.
- fixing of $f(x_b)$.

The validity of the filtering in coordinate space in the present case is supported by calculations over a wider range of connection points x_0 as shown in the following. There and in the above comparison, $f(x_b) = 10^{-8}$ and $c = 1\mu m$ were chosen.

3.1.4 Calculation of the Reflectivity and Comparison of Methods

Having introduced absorbing boundaries, the reflectivity was then calculated from the evolution of a wave packet in the potential. The reflectivity was computed for different values of the connection point x_0 and for different spatial step sizes Δx. The results are shown and compared to those obtained by an integration of the *stationary* Schrödinger equation in Fig. 9.

All calculations are consistent with the time-independent calculation till x_0 reaches approximately $7 \cdot 10^{-10}m$. There, the calculation with $N = 2^{16}$ grid points breaks down. The calculation with $N = 2^{17}$ is valid until $x_0 \approx 4 \cdot 10^{-10}m$, whereas with $N = 2^{18}$ grid points it was possible to reach still smaller values of x_0. This behavior is understandable, since the $-C_3/x^3$-potential falls rapidly for small values of x. As x_0 becomes smaller, the wave function gains more energy which results in fast oscillations. A smaller step size Δx is needed to represent those effects; if the step size is too large to represent the oscillations of the wave function, it is completely reflected, as seen in Fig. 9. It has to be pointed out that the calculation with $N = 2^{19}$ grid points differs from the reference curve for $x_0 < 2 \cdot 10^{-10}m$ without reaching a reflectivity of 1. Here, the reason for the deviation is due to the used absorbing mask, which fails to absorb the high energies occurring in this regime[3].

[3]This can be seen in the calculated distribution of the particle, where reflections are visible for $x_0 < 2 \cdot 10^{-10}m$.

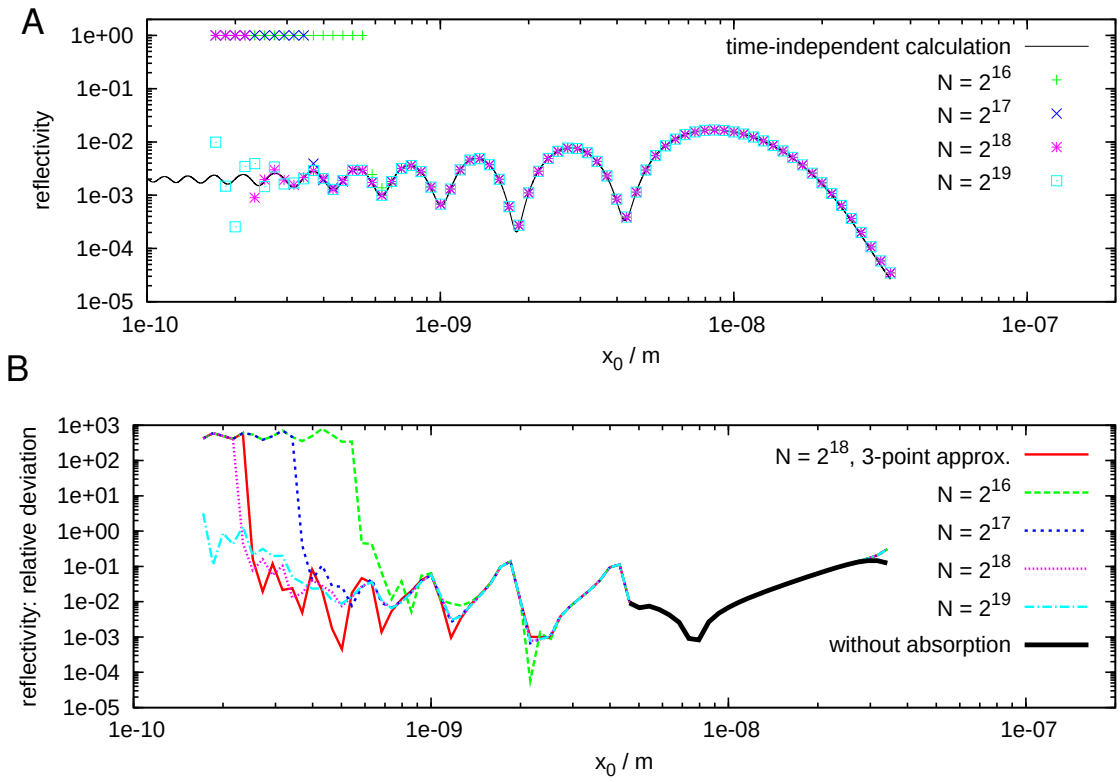

Figure 9: Calculations of the reflectivity. A: The reflectivity is shown in dependence of the connection point x_0. The calculations have been carried out for different numbers of grid points N on a box of size $6.6\mu m$. B: The relative deviation $|\frac{R-R_0}{R_0}|$ to the value R_0 obtained by an integration of the stationary Schrödinger equation is shown. The calculations carried out with the *five-point approximation* are shown here. The red curve in figure B was obtained by a *three point approximation*. For the black curve in figure B, no absorbing boundaries were used.

The relative deviation to the reference curve was calculated (Fig. 9B). For values of x_0 where the absorbing boundary is not necessarily needed, data obtained without an absorbing boundary is shown. Except for the right end of the curve, the data agrees, which indicates the validity of the used absorbing mask for the range

$$3 \cdot 10^{-10} m < x_0 < 2 \cdot 10^{-8} m. \tag{18}$$

Furthermore, a curve calculated with the *three-point approximation* and 2^{18}-grid points is shown for comparison to the *five-point approximation*. One can infer the following: The three-point approximation fails slightly before the five-point approx-

imation, because the latter is more accurate in estimating the derivative of the wave function by two orders in Δx. For higher x_0, however, both approximations yield comparable results, which means that the precision of the three-point approximation ($\mathcal{O}(\Delta x^2)$) is sufficient in that regime. Both the three-point approximation and the five-point approximation have been investigated with respect to their computational costs (computation time for one simulation). The results are given in appendix C.

In the range $5 \cdot 10^{-10} \leq x_0 \leq 10^{-8}$, the relative deviation is bounded by approximately 10%. Larger relative deviations coincide with smaller absolute values of the reflectivity. The averaged relative deviation for the calculation with 2^{17} grid points is 2.3%, which can be seen as an estimate of the accuracy of the method.

3.2 Time-Dependent Potential

As an application, a non-static potential was considered. Therefore, the time-dependent potential

$$W(x,t) = V(x - A\sin(\omega t)), \tag{19}$$

which describes a harmonically oscillating surface, was introduced (A: amplitude of the oscillation, ω: angular frequency, V: $-C_3/x^3$-potential with the parabolic continuation). Due to the oscillations of the surface, an energy transfer from the surface to the particle may happen. Since the scale of the energy transfer is given by $\hbar\omega$, it can influence the dynamics of the particle if the frequency ω is of the order of

$$\omega_{in} = E/\hbar \tag{20}$$

(E: energy of the particle, $\omega_{in} = 9.4981 \cdot 10^7 1/s$ for $v = -2m/s$).

3.2.1 Momentum Distribution

For different values of the oscillation frequency ω, the distribution of the reflected particle in coordinate and in momentum space was calculated (Fig. 10).

For $\omega = 0.01\omega_{in}$, no effects are visible, whereas for $\omega = 0.1\omega_{in}$, distortions begin to appear in the distributions. When ω reaches ω_{in}, sidebands to the central peak in the momentum distribution are clearly visible. If the oscillation frequency is increased further, only the right side peaks remain, because the left side peak then corresponds

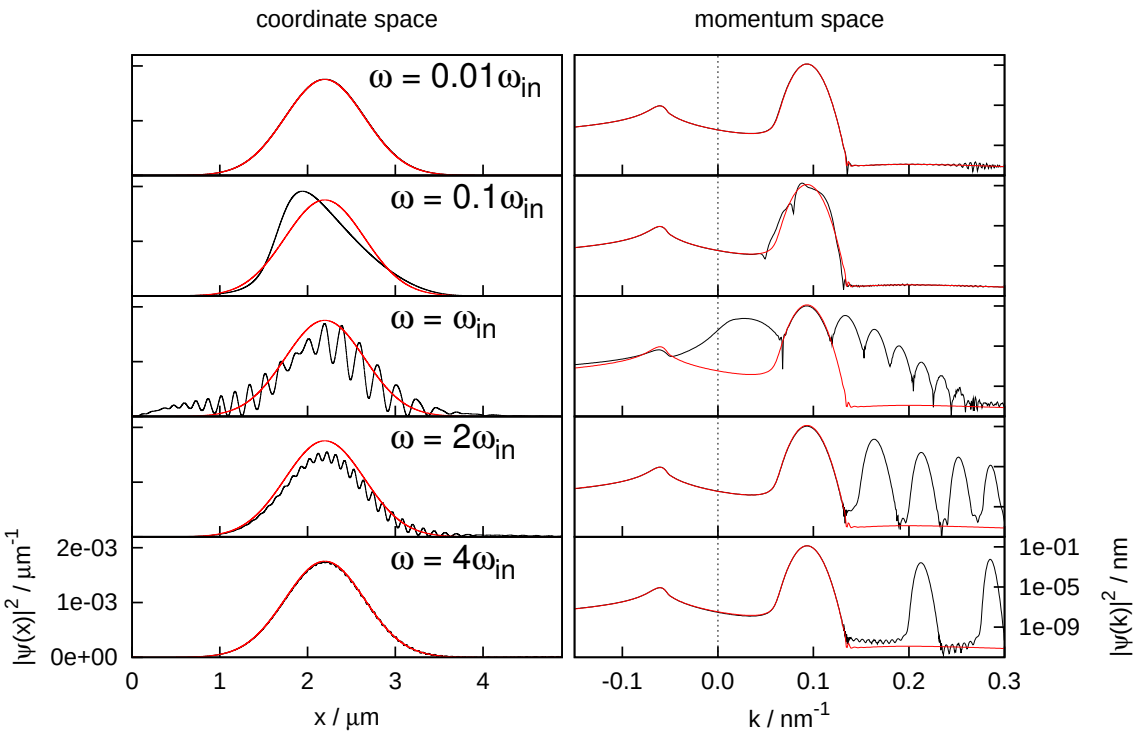

Figure 10: Coordinate and momentum distribution for a particle reflected on the oscillating surface (amplitude $A = 4.0nm$) for different frequencies ω (black curve). Red curve: corresponding distributions without oscillations. (Numerical parameters: connection point: $-C_3/x_0^3 = -10^{-23}J$, three-point-approx. and absorbing boundaries. For $\omega = \omega_{in}$: 2^{18} grid points, $\Delta t = 10^{-10}s$, size of the numerical box: $9\mu m$. For $\omega = 2\omega_{in}$ and $\omega = 4\omega_{in}$, the time step has been made smaller according to the increase in the frequency and the size of the box has been increased using 2^{19} grid points.)

to a *negative* momentum, i.e. to a transmitted particle, which is absorbed by the boundary. The right peaks lie further away from the central peak as for smaller frequencies. This shows that the energy transfer becomes larger. In the coordinate distributions, significant oscillations imprinted by the surface are visible for $\omega \geq \omega_{in}$.

It might be surprising that the maximum of the left side band for $\omega = \omega_{in}$ does not lie at 0. This effect can be understood by taking into account the relation between energy and momentum: Due to the energy absorption of $\hbar\omega_{in}$, there is a raised probability that the particle has the energy $E = 0$ (i.e. the energy distribution has a local maximum at 0). Since the energy E is proportional to k^2 it follows that $\mathrm{d}E \propto k\,\mathrm{d}k$. Compared to the energy distribution, the momentum distribution is

therefore multiplied by k, i.e. the maximum at $E = 0$ is damped and shifted to positive values. Negative values of k correspond to a transmitted particle, which is accelerated further and absorbed. Therefore, the peak corresponding to an energy absorption of $\hbar\omega_{in}$ is only visible for positive values of k.

The case $\omega = \omega_{in}$ was expected to differ qualitatively from the other cases due to resonance effects (for example by an increased level of disorder in coordinate space). It remains an open question why this expectation was not fulfilled.

3.2.2 Sidebands in the Energy Distribution

As a next step, the energy distribution of the reflected particle was investigated. The energy transfer due to the oscillation of the surface was expected to be quantized by integer multiples of $\hbar\omega$:

$$E_n = \hbar\omega_{in} + n\hbar\omega. \tag{21}$$

Therefore, it was convenient to consider the distribution $\rho(k)\,\mathrm{d}k \equiv |\psi(k)|^2\,\mathrm{d}k$ as a function of the new variable

$$z = \frac{\frac{\hbar^2 k^2}{2m} - \hbar\omega_{in}}{\hbar\omega}, \tag{22}$$

$$\rho(k)\,\mathrm{d}k = \rho(k)\frac{m\omega}{\hbar k}\,\mathrm{d}z. \tag{23}$$

The peaks in this (scaled and shifted) energy distribution are then expected to be at integer values of z. As shown in Fig. 11, this expectation is basically fulfilled. It is confirmed that the left side band, which exists for $\omega = \omega_{in}$, is shifted to the left when considering the energy distribution. The following table contains the positions of the maxima which have been red off from the distributions:

expected position of max.	-1	0	1	2	3	4	
	-0.97	-0.05	0.96	1.97	2.97	4.02	$\omega = \omega_{in}$
position of max.	———	-0.02	0.98	2.01	3.01	4.01	$\omega = 2\omega_{in}$
	———	-0.01	1.00	2.00	3.00	4.00	$\omega = 4\omega_{in}$

The following reasons are suggested for the slight deviations from the expectation: It might be that the idea of the particle absorbing exact multiples of $\hbar\omega$ is limited; the deviations might be caused by the mixing of several absorption processes of different order. Another possible reason might be that the peaks lie on top of a

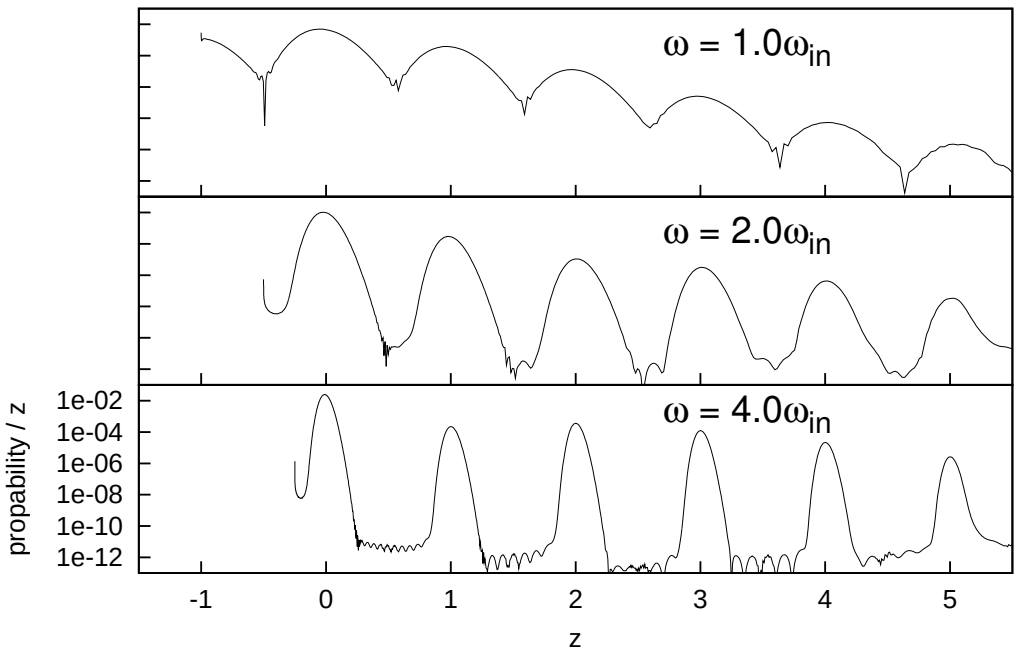

Figure 11: Rescaled and shifted energy distribution. This distribution has been computed from the momentum distribution for positive momenta k (Fig. 10). For each value of ω, the variable z has been introduced such that the expected peaks are at integer values. For all curves, the amplitude is $A = 4nm$.

background, which shifts their positions (for $z > 0$) slightly to the left. Finally, one has to take into account that all peaks have a finite width. In the above table, only the maximum was indicated.

3.2.3 Optimization of Numerical Parameters

For the case $\omega = \omega_{in}$, the reflectivity for the different peaks in the momentum distribution was calculated separately for a range of values of x_0. In the following, we refer to the central, elastic peak as that of order $n = 0$, whereas the side peaks are labeled by $n = -1$ (left) and $n = 1, 2$ (right). Without absorbing boundaries, it was first checked that the numerical parameters Δx and Δt are chosen appropriately (Fig. 12). Then, absorbing boundaries were used to reach smaller values of x_0.

In Fig. 13, the results for a computation with different values of x_0 are shown. The reflectivity was calculated for the orders $n = -1, 0, 1, 2$. Qualitatively, the reflectivity shows the same oscillating behavior as for the static potential. Furthermore, the dependence on the number of grid points N, as observed in the stationary case, is recovered. It is confirmed that the five-point and the three-point approximations

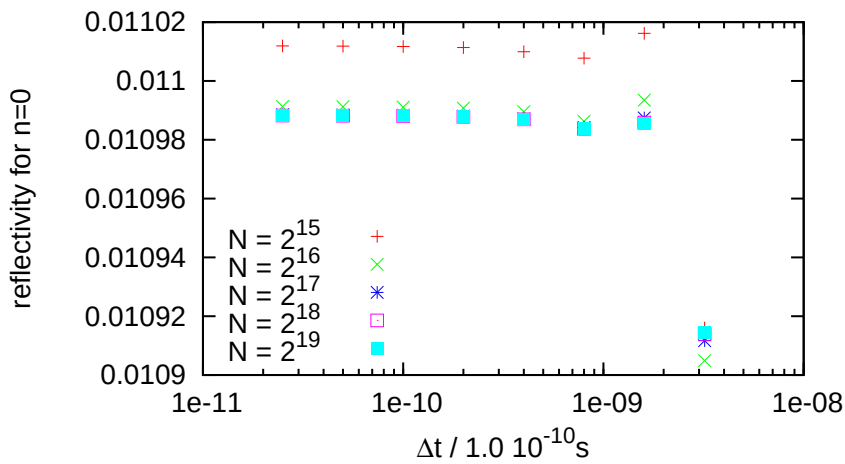

Figure 12: Optimization of numerical parameters for the time-dependent potential W(x,t) with an amplitude of $A = 4nm$ and $\omega = \omega_{in}$. The reflectivity for the central peak ($n = 0$) of the momentum distribution is shown. It was concluded that $N \geq 2^{17}$ and $\Delta t \leq 1 \cdot 10^{-10} s$ should be chosen. (Size of the numerical box: $15.5\mu m$, connection point: $-C_3/x_0^3 = -10^{-25} J$, three-point-approx., no absorbing boundaries)

yield equal results for a large range of values of x_0. Where possible, the calculation was also carried out without using absorbing boundaries. The accordance of the calculations confirms the validity of the used absorbing technique.

3.2.4 Limit of Small x_0

With this information, values of the reflectivity for each peak as $x_0 \to 0$ could be obtained. Therefore, 300 calculations over the range $3.44 \cdot 10^{-10} m < x_0 < 3.42 \cdot 10^{-9} m$ were carried out. Averages over R as a function of x_0 were obtained according to

$$R_{avg} = \exp\left(\frac{1}{\ln y_2 - \ln y_1} \int_{\ln y_1}^{\ln y_2} \ln(R(\exp y))\, \mathrm{d}y\right), \tag{24}$$

i.e. the averaging was carried out on the double-logarithmic scale. It has been found out, that this averaging on the double-logarithmic scale converges faster against a final value than averaging on the linear scale[4]. Averages were calculated between subsequent maxima of $R(x_0)$ as shown in Fig. 14.

The last average (for the lowest values of x_0), was taken as the final value of the

[4]G. Łach, private communication.

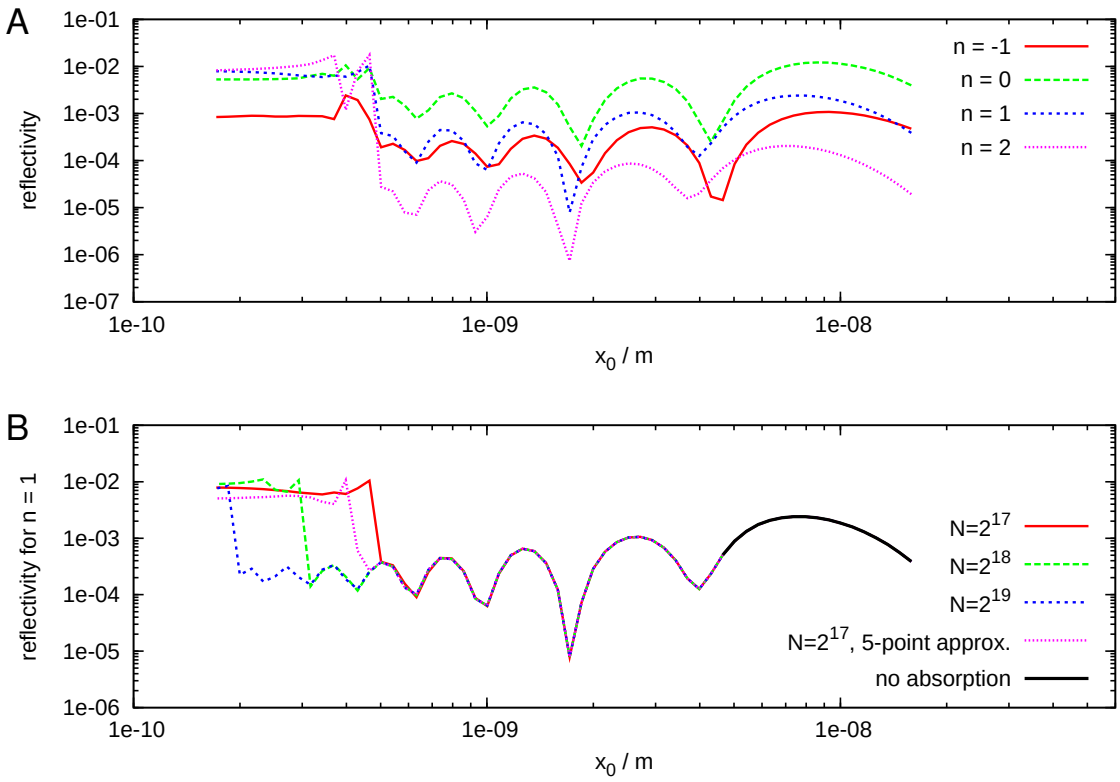

Figure 13: Reflectivity for peaks of different order as a function of x_0. A: The reflectivity is shown for all orders. B: The reflectivity for the order $n = 1$ is shown for different numbers of grid points. The three-point approximation is used except for one curve. (Size of the numerical box: $9\mu m$, $\Delta t = 10^{-10}s$). A curve computed without absorbing boundaries is added (black).

reflectivity. The mean velocity for each peak was calculated by fitting Gaussian functions to the peaks in the momentum distribution. Then, as for the reflectivity, averages were taken. For

$$v = \quad -2m/s \quad : \text{initial mean velocity of the particle} \tag{25}$$

$$\omega = 9.4981 \cdot 10^7 1/s: \text{angular frequency of the oscillation} \tag{26}$$

$$A = \quad 4.0nm \quad : \text{amplitude of the oscillation} \tag{27}$$

the following results were obtained:

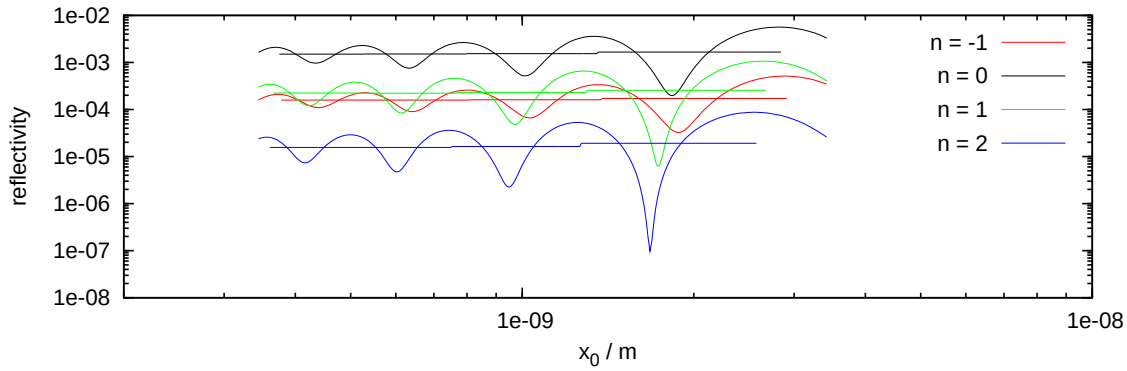

Figure 14: Reflectivity as a function of x_0 and averages. The averages were taken between subsequent maxima on the double-logarithmic scale. (numerical parameters: 2^{19} grid points for larger values of x_0, 2^{20} grid points for smaller values of x_0, size of the numerical box: $9\mu m$, $\Delta t = 10^{-10}s$.)

order of the peak	$n = -1$	$n = 0$	$n = 1$	$n = 2$
reflectivity	0.000159	0.0015	0.00022	$1.57 \cdot 10^{-5}$
reflectivity relative to $n = 0$	0.11	1.00	0.15	0.010
mean velocity in m/s	0.594	1.97	2.82	3.46

The mean velocity of the central peak ($n = 0$) is expected to coincide with the mean incident velocity. This expectation is fulfilled up to the small deviation of $0.03m/s$. The standard deviation of the fitted Gaussian functions is $0.13m/s$, i.e. it is 4.3 times larger than the deviation of $0.03m/s$. Furthermore, the minimal momentum which can be represented by the numerical grid corresponds to $0.015m/s$, which is of the same order than the deviation. It cannot be excluded that numerical errors are the reason for the deviation.

4 Conclusion and Perspectives

In this project, the reflection of a particle in a $-C_3/x^3$-potential, which describes atom-surface interactions, was studied. To make the numerical treatment of the problem possible, the potential was cut at some $x_0 > 0$ and suitably continued. This allowed the transmitted particle to move to $x \to -\infty$. It was argued that in the limit $x_0 \to 0$, the physical situation is recovered. Because of artificial reflections at the boundary of the numerical grid, absorbing boundaries were introduced. The comparison of different methods showed that for the present case, an absorption in coordinate space via a damping function has to be preferred. By comparison to calculations carried out within the time-independent Schrödinger equation, the numerical parameters were optimized and the validity of the absorbing boundaries was checked. In this way, it was possible to reach a regime of connection points x_0 from which the actual reflectivity was extrapolated by averaging.

With the method applied and tested in this project, the dynamics of a particle being reflected on a surface can be investigated in the direction perpendicular to the surface. A recent experiment [12] suggests that, for large perpendicular velocities, the reflectivity is also influenced by the velocity component parallel to the surface. It might therefore be interesting to extend the method to the second dimension. The obtained results include that, for one dimension, 2^{17} grid points are necessary. Assuming an overall maximum of approximately 2^{30} grid points, this leaves approximately 2^{13} grid points for the second dimension, which might be worth considering.

As an application of the one-dimensional method, the reflection of an atom on a periodically oscillating surface was studied. It was shown, that the momentum distribution of the reflected particle is changed if the oscillation frequency is of the order of the particle's energy. In this case, side peaks arise in the momentum distribution in addition to the elastic peak. By considering the energy distribution, it could be verified that the energy transfer corresponds to integer multiples of the oscillation frequency. For one case, the reflectivity for the elastic peak and for three side peaks was calculated. On the whole, it was shown, that the peaks neighboring the central peak reach a reflectivity of roughly 10% of the latter.

According to [4], the commercially available oscillating membrane has a critical amplitude of $3.5nm$ and a frequency of $\omega = 2\pi \cdot 133784/s$ (fundamental frequency). It might be interesting to test the effect discussed in this project experimentally, since experiments considering quantum reflection on an oscillating surface are un-

known to the author. The critical amplitude of the available membrane is close to $4nm$, which was used here. An incoming ^3He particle must have a velocity of approximately $0.188m/s$ ($k \approx 0.000473a.u.$) to fulfill the condition $\omega_{in} = \omega$ for the available membrane. Here, the calculations were carried out for higher velocities and frequencies. Yet, the effect is expected to occur also for lower frequencies, which could be tested by further numerical calculations.

A Crank-Nichelson Method for the Schrödinger Equation

The numerical method, which was used here, is the *Crank-Nichelson* method for the Schrödinger equation. The following explanations are based on [9, p. 640 - 652]. An approximation of the time evolution operator $U_{t,t'} = \exp(-iH \cdot (t-t')/\hbar)$ serves as a starting point for the numerics[5]: Given a state $\psi_{t'}$ at time t', a solution to the Schrödinger equation

$$i\hbar \frac{\partial \psi_t}{\partial t} = H\psi_t \tag{28}$$

for the time t is given by $\psi_t = U_{t,t'}\psi_{t'} = \exp(-iH \cdot (t-t')/\hbar)\psi_{t'}$. From there, it follows that

$$e^{iH\Delta t/2\hbar}\psi_{t+\Delta t} = e^{-iH\Delta t/2\hbar}\psi_t, \tag{29}$$

where Δt is a time step. If Δt is small enough, this can be approximated by

$$(1 + iH\Delta t/2\hbar)\psi_{t+\Delta t} = (1 - iH\Delta t/2\hbar)\psi_t. \tag{30}$$

In order to solve Eq. (30) numerically, a spatial discretization and a discretization in time is introduced, whereby the wave function $\psi_t(x)$ is sampled at discrete points:

$$\psi_k^j = \psi_{k\Delta t}(x^j). \tag{31}$$

Here $j = 1 \dots N$ denotes a spatial index, k denotes an index in time, $x^j = x_{min} + j \cdot \Delta x$, where x_{min} is the lower boundary of the numerical grid, and Δx the spatial step size.

Originally acting on the space of physical states, operators need to be mapped to $N \times N$-matrices, i.e. to operators acting on discretized wave functions. In order to represent the kinetic part of the Hamiltonian, a discrete approximation of the

[5] For a time-dependent Hamiltonian $H(t)$ as considered in section 3.2, the time-evolution operator U is the time-ordered exponential [13]

$$U_{t,t'} = T\exp(-i/\hbar \cdot \int_{t'}^{t} H(\tau)\,\mathrm{d}\tau).$$

The first order approximation of $U_{t,t'}$, which is used in the numerical method, is the same as for a time-independent Hamiltonian, apart from H now being evaluated at t': $U_{t,t'} \approx 1 - i(t-t') \cdot H(t')/\hbar$.

second derivative $\partial^2/\partial x^2$ is necessary. Here, the approximations

$$\frac{\partial^2\psi}{\partial x^2}(x^j) = \frac{\psi(x^{j-1}) - 2\psi(x^j) + \psi(x^{j+1})}{(\Delta x)^2} + \mathcal{O}(\Delta x^2) \quad \text{and} \tag{32}$$

$$\frac{\partial^2\psi}{\partial x^2}(x^j) = \frac{-\psi(x^{j-2}) + 16\psi(x^{j-1}) - 30\psi(x^j) + 16\psi(x^{j+1}) - \psi(x^{j+2})}{12(\Delta x)^2} + \mathcal{O}(\Delta x^4) \tag{33}$$

were used [14].

The first approximation (*three-point approximation*) gives rise to tridiagonal matrices as representations of the operators in Eq. (30) and the second approximation (*five-point approximation*) leads to five-diagonal matrices.

Having introduced this dicretization, the equation

$$A_2\psi_{t+\Delta t} = A_1\psi_t \tag{34}$$

was solved for each time step. Here, A_2 and A_1 are the matrix representations of $1 + iH\Delta t/2\hbar$ and $1 - iH\Delta t/2\hbar$, respectively. For a tridiagonal A_2, the equation was solved by a Gaussian elimination [15], for a five-diagonal A_2, an LL^t-decomposition of A_2 was carried out and $\psi_{t+\Delta t}$ was calculated by back substitution [16, 17].

B Time-Independent Calculation of the Reflectivity

The stationary Schrödinger equation

$$-\frac{\hbar^2}{2m}\frac{\mathrm{d}^2\psi}{\mathrm{d}x^2}(x) + V(x)\psi(x) = E\psi(x) \tag{35}$$

was solved for the $-C_3/x^3$-potential with one of the continuations described in section 2.1. To do so, an initial condition $(\psi(x_i), \psi'(x_i))$ was specified where $\psi(x)$ is known analytically. Then, $(\psi(x_f), \psi'(x_f)$ was calculated numerically for a point x_f, where the potential $-C_3/x^3$ is sufficiently close to 0. At x_f, the wave function must then be of the form

$$\psi(x) = Ae^{ikx} + Be^{-ikx}, \tag{36}$$

with complex constants A and B, and the reflectivity R is given by (see section 1.1):

$$R = |\frac{A}{B}|^2. \tag{37}$$

R was thus calculated by solving

$$\psi(x_f) = Ae^{ikx_f} + Be^{-ikx_f} \tag{38}$$

$$\psi'(x_f) = ikAe^{ikx_f} - iBke^{-ikx_f} \tag{39}$$

for A and B.

The initial condition $(\psi(x_i), \psi'(x_i))$ was chosen such that ψ represents an *outgoing* particle for $x \to -\infty$. In the case of the *constant* and the *parabolic continuations*, the potential reaches constant values, namely $-C_3/x_0^3$ for $x \leq x_0$ (constant continuation) and $-2.5 \cdot C_3/x_0^3$ for $x \leq 0$ (parabolic continuation). Let k' be the wave vector of the particle in that region. Then

$$\psi(x) = e^{-ik'x} \tag{40}$$

has the desired boundary condition[6]. This allowed to specify the initial condition as

$$\psi(x_i) = e^{-ik'x_i} \tag{41}$$

$$\psi'(x_i) = -ik'e^{-ik'x_i}. \tag{42}$$

In a next step, the *linear continuation* was considered, i.e. $V(x) = \alpha x + \beta$ for $x \leq x_0$ and with real constants $\alpha > 0$ and $\beta < 0$ according to Eq. (8). A treatment of this problem can be found in [5, p. 72-74]: Introducing the variable transformation

$$\xi = (\frac{2m\alpha}{\hbar^2})^{\frac{1}{3}}(x - \frac{\beta - E}{\alpha}) \tag{43}$$

the Schrödinger equation reads

$$\frac{\mathrm{d}^2\psi}{\mathrm{d}\xi^2}(\xi) = \xi\psi(\xi), \tag{44}$$

which is the *Airy differential equation*[18, p. 446]. Therefore, $\psi(\xi)$ is a linear

[6]One is free to multiply the term $\exp(-ik'x)$ by any complex constant $C \neq 0$, since then the whole solution to the Schrödinger equation is multiplied by that constant, which drops out in the expression for the reflectivity: $R = |(CA)/(CB)|^2 = |A/B|^2$

combination of the Airy functions of the first and the second kind, $\mathrm{Ai}(\xi)$ and $\mathrm{Bi}(\xi)$. In the case considered in [5], only Ai is chosen since Bi is unbounded for $\xi \to \infty$. Here, however, the linear potential was only considered for $x \leq x_0$ and Bi was kept. Changing to the basis $f \equiv \mathrm{Bi} + i\mathrm{Ai}$ and $g \equiv \mathrm{Bi} - i\mathrm{Ai}$, ψ is of the form

$$\psi(\xi) = \lambda f(\xi) + \mu g(\xi), \tag{45}$$

with complex constants λ, μ. Using the known asymptotic expressions of Ai and Bi[18, p. 448,449] for $\xi \to -\infty$, it follows that

$$f(\xi) \underset{\xi \to -\infty}{\sim} \frac{i}{\sqrt{\pi}(-\xi)^{1/4}} e^{i\frac{2}{3}(-\xi)^{3/2}} \tag{46}$$

$$g(\xi) \underset{\xi \to -\infty}{\sim} \frac{-i}{\sqrt{\pi}(-\xi)^{1/4}} e^{-i\frac{2}{3}(-\xi)^{3/2}}. \tag{47}$$

These expressions were used to calculate the asymptotic form of the probability flux as

$$j_\psi(x) = \frac{\hbar}{m} \mathrm{Im}(\psi^* \frac{\mathrm{d}\psi}{\mathrm{d}x}) \tag{48}$$

$$\underset{x \to -\infty}{\sim} \frac{\hbar}{\pi m} (\frac{2m\alpha}{\hbar^2})^{\frac{1}{3}} (|\mu|^2 - |\lambda|^2). \tag{49}$$

Therefore, $\lambda \cdot f$ contributes a *negative* term to the asymptotic flux, whereas $\mu \cdot g$ contributes a *positive* term. The *outgoing* particle is thus represented by $f = \mathrm{Bi} + i\mathrm{Ai}$. This allowed to use

$$\psi(x_i) = \mathrm{Bi}(\xi(x_i)) + i\mathrm{Ai}(\xi(x_i)) \tag{50}$$

$$\psi'(x_i) = \mathrm{Bi}'(\xi(x_i)) + i\mathrm{Ai}'(\xi(x_i)) \tag{51}$$

as an initial condition for the numerical integration[7].

C Computational Costs: Computation Time

In order to estimate the time, which is needed to run longer calculations, it is useful to know, how the computation time depends on the number of spatial grid points. This was investigated for the five-point and the three-point approximation and is illustrated in Fig. 15.

[7] As above, there is the freedom of a multiplicative constant and $\lambda = 1$ was chosen.

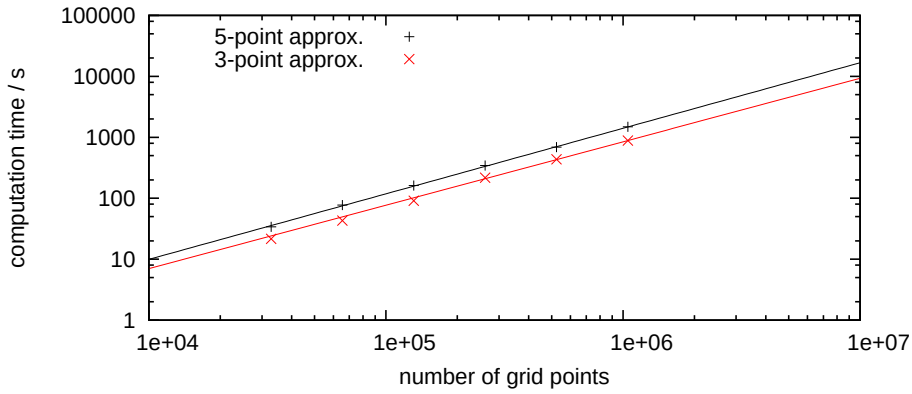

Figure 15: Computation time. The computations were carried out with 18000 time steps on a $3GHz$-CPU. The solid lines are fitted power law curves.

The following dependency was obtained by power law fits:

$$T/sec. = 0.0050 \cdot N^{1.08} \tag{52}$$

$$T/sec. = 0.0048 \cdot N^{1.04}. \tag{53}$$

Here, T is the computation time for 18000 time steps and N is the number of spatial grid points. This analysis shows that calculations with the three-point approximation are faster than with the five-point approximation. The reason for this is that the latter requires more steps of computation to calculate $\psi_{t+\Delta t}$ out of ψ_t, since the involved matrices contain two more off-diagonals.

In general, the five-point approximation is expected to represent the second derivative of the wave function better than the three-point approximation, if the wave function is oscillating fast. For the $-C_3/x^3$-potential, this is the case for very small values of x. Then, the three-point approximation requires a larger number of grid points to reach the accuracy of the five-point approximation. In this case, the five-point approximation is advantageous since it allows to use less grid points, which then saves computation time. Apparently, this regime was not reached in the calculations carried out in this project. Here, both approximations are basically equivalent, as shown in section 3.1.4.

D Retarded Potential

For all presented calculations, the retardation term $-C_4/x^4$ was not taken into account. It was checked that the method also applies for the extended potential, i.e.

for

$$V(x) = -\frac{C_4}{x^3(x+l)}. \tag{54}$$

The calculations, shown in Fig. 16, were carried out with $l = 93 \cdot 10^{-10} m$, which applies for helium [7].

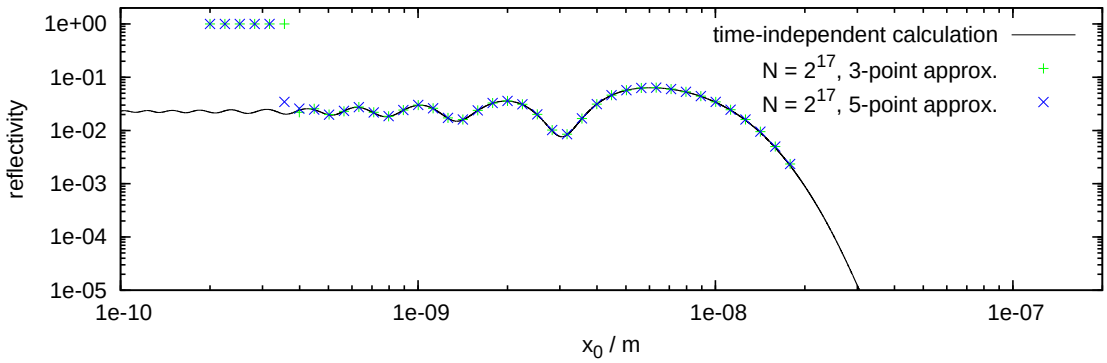

Figure 16: Calculations for the extended potential. A parabolic continuation for $x < x_0$ was used. (Size of the numerical box: $6.6\mu m$, $\Delta t = 2 \cdot 10^{-10} s$)

E References

[1] F. Shimizu, Phys. Rev. Lett. **86**, 987 (2001).

[2] J. Madroñero and H. Friedrich, Phys. Rev. A **75**, 022902 (2007).

[3] P. L. Garrido, S. Goldstein, J. Lukkarinen, and R. Tumulka, ArXiv e-prints (2008), 0808.0610.

[4] B. M. Zwickl *et al.*, Applied Physics Letters **92**, 103125 (2008), 0711.2263.

[5] L. D. Landau and E. M. Lifschitz, *Quantenmechanik* (Akademie-Verlag, Berlin, 1984).

[6] J. F. Babb, Journal of Physics: Conference Series **19**, 1 (2005).

[7] G. Lach, M. Dekieviet, and U. D. Jentschura, Int. J. Mod. Phys. **A25**, 2337 (2010).

[8] G. Audi and A. H. Wapstra, Nuclear Physics A **595**, 409 (1995).

[9] W. H. Press, B. P. Flannery, S. A. Teukolsky, and W. T. Vetterling, *Numerical recipes*, Repr. ed. (Cambridge Univ. Pr., Cambridge, 1988).

[10] E. Jones *et al.*, SciPy: Open source scientific tools for Python, 2001–2011.

[11] T. Shibata, Phys. Rev. B **43**, 6760 (1991).

[12] B. S. Zhao, H. C. Schewe, G. Meijer, and W. Schöllkopf, Phys. Rev. Lett. **105**, 133203 (2010).

[13] F. Schwabl, *Quantenmechanik*, 7. aufl. ed. (Springer, Berlin; Heidelberg [u.a.], 2007).

[14] B. Fornberg, Math. Comp. **51**, 699 (1988).

[15] J. Stoer, *Numerische Mathematik 1:* (Springer, 2005).

[16] G. Golub and C. Loan, *Matrix computations* (Johns Hopkins University Press, 1996).

[17] R. A. Horn and C. R. Johnson, *Matrix analysis*, 21. print. ed. (Cambridge Univ. Press, Cambridge [u.a.], 2007).

[18] M. Abramowitz and I. A. Stegun, *Handbook of Mathematical Functions with Formulas, Graphs, and Mathematical Tables*, ninth dover printing, tenth gpo printing ed. (Dover, New York, 1964).

Erklärung

Ich versichere, dass ich diese Arbeit selbstständig verfasst und keine anderen als die angegebenen Quellen und Hilfsmittel benutzt habe.

Heidelberg, den 18.07.2011,

(Benedikt Herwerth)